



## Microstructure and properties of rheo-HPDC Al–8Si alloy prepared by air-cooled stirring rod process

Ming-fan QI<sup>1</sup>, Yong-lin KANG<sup>1,2</sup>, Guo-ming ZHU<sup>1</sup>

1. School of Materials Science and Engineering, University of Science and Technology Beijing, Beijing 100083, China;

2. Key Laboratory for Advanced Materials Processing of Ministry of Education, University of Science and Technology Beijing, Beijing 100083, China

Received 27 November 2016; accepted 25 May 2017

**Abstract:** A new and effective semisolid slurry preparation process with air-cooled stirring rod (ACSR) is reported, in which the compressed air is constantly injected into the inner cavity of a stirring rod to cool the melt. The slurry of a newly developed high thermal conductivity Al–8Si alloy was prepared, and thin-wall heat dissipation shells were produced by the ACSR process combined with a HPDC machine. The effects of the air flow on the morphology of  $\alpha_1$ -Al particles, mechanical properties and thermal conductivity of rheo-HPDC samples were studied. The results show that the excellent slurry of the alloy could be obtained with the air flow exceeding 3 L/s. Rheo-HPDC samples that were produced with the air flow of 5 L/s had the maximum UTS, YS, elongation, hardness and thermal conductivity of 261 MPa, 124 MPa, 4.9%, HV 99 and 153 W/(m·K), respectively. Rheo-HPDC samples show improved properties compared to those formed by HPDC, and the increasing rates of UTS, YS, elongation, hardness and thermal conductivity were 20%, 15%, 88%, 13% and 10%, respectively.

**Key words:** rheo-HPDC; Al–8Si alloy; air-cooled stirring rod; microstructure; mechanical properties; thermal conductivity

### 1 Introduction

In past years, in order to provide solutions for environmental and energy problems, the importance of Al alloys as lightweight metals has been recognized, especially in fields of communication and automotive applications [1–3]. High pressure die-casting (HPDC) technology is one of the most widely employed manufacturing processes for producing Al alloy parts, where the primary advantages are high productivity and the casting of components with thin walls and complex geometries [4]. However, HPDC Al alloys for safe critical parts are restricted due to internal defects and corresponding reductions in material performance [4–6].

Improvement of the HPDC process to form parts with high quality and increased performance is thus highly worthwhile. Rheo-HPDC process has the capability to produce high quality parts [7–9]. Semisolid slurry preparation is an important process for rheo-HPDC [10–12]. Some of slurry preparation methods, such as serpentine channel pouring process [8,13], vacuum-assisted electromagnetic stirring process [14]

and gas bubbling process [15], appeared. However, some disadvantages exist in these methods, such as difficulties in cleaning and the complicated disassembly and installation of the devices, limiting wide utilization in industrial applications [11,16,17].

In order to solve the issues that exist in the slurry preparation, a new and effective air-cooled stirring rod (ACSR) device was designed. In this work, semisolid slurry of a newly developed high thermal conductivity hypoeutectic Al–8Si alloy was prepared by ACSR process and thin-wall heat dissipation shells for wireless base station were formed by ACSR combined with a HPDC machine. The effects of the air flow on the microstructure, mechanical properties and thermal conductivity of rheo-HPDC parts were studied.

### 2 Experimental

Al–8Si alloy, as a newly developed high thermal conductivity hypoeutectic Al–Si alloy, was used in semisolid forming in this study. The main chemical compositions of the alloy were Si 7.73%, Fe 0.53%, Mg 0.03%, Zn 0.02% and Al balance (mass fraction). The

liquidus and solidus were 625 and 565 °C, respectively, measured by differential scanning calorimetric (DSC) method, as shown in Fig. 1(a). The relationship between temperature and solid fraction of the alloy was acquired by calculating the area ratio of DSC curves, as shown in Fig. 1(b). It can be found that the alloy is suited to semisolid forming due to a wider solid–liquid range and smooth change of solid fraction versus temperature.

The experiment was carried out by utilizing a self-developed ACSR solidification setup. A sketch map of the apparatus is shown in Fig. 2. The apparatus mainly

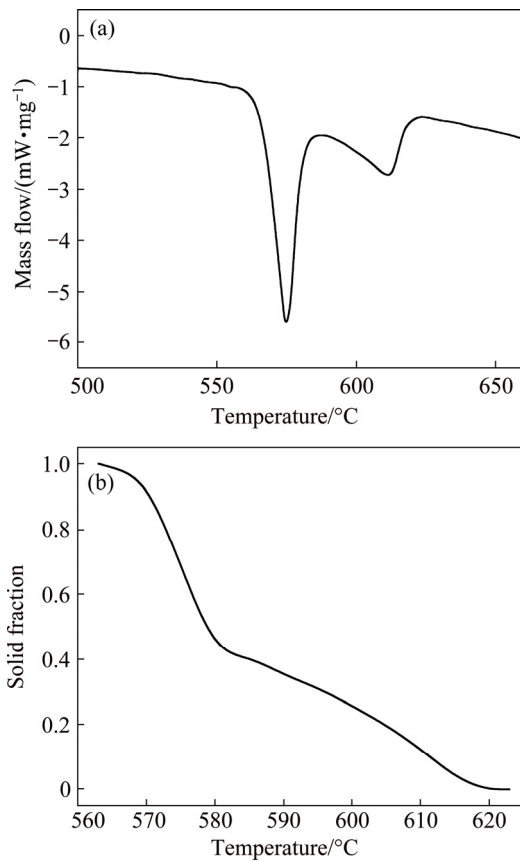


**Fig. 1** DSC results of Al-8Si alloy (a) and variation of solid fraction against temperature (b)

consisted of air compressor, airway, stirring rod, thermocouple, etc. The chosen material of the stirring rod was SKD61 die steel treated by nitriding. The air, generated from the air compressor, was constantly injected into the inner cavity of stirring rod through the airway to cooling the melt. During the slurry preparation, the air flow was adjusted to 0–5 L/s at the pouring temperature of 660 °C, stirring speed of 800 r/min and stirring time of 25 s. Al-8Si alloy was melted in a top-loading resistance furnace at 720 °C. The melt was cooled to 660 °C after degassing. Then, about 5.5 kg of the melt were poured into the crucible and treated by ACSR. After being treated for 25 s, some slurry was scooped by a clay crucible with the inner diameter of 50 mm and quenched in water immediately, and the remaining slurry was shaped by a cold chamber HPDC machine to produce thin wall heat dissipation shells. The photographs of the shells are presented in Fig. 3. For comparison, conventional HPDC samples were prepared at a pouring temperature of 660 °C. The mechanical

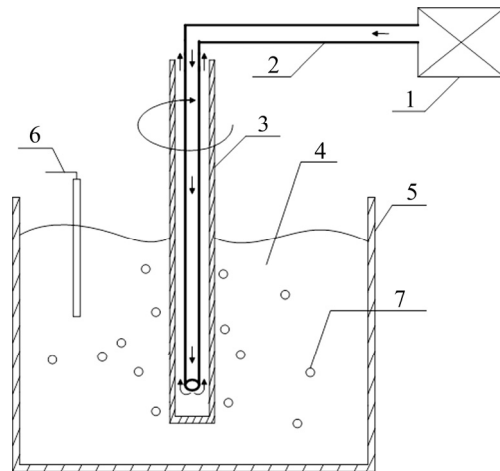


**Fig. 2** Sketch map of ACSR apparatus (1—Air compressor; 2—Airway; 3—Stirring rod; 4—Melt; 5—Crucible; 6—Thermocouple; 7—Primary  $\alpha$ -Al particle)

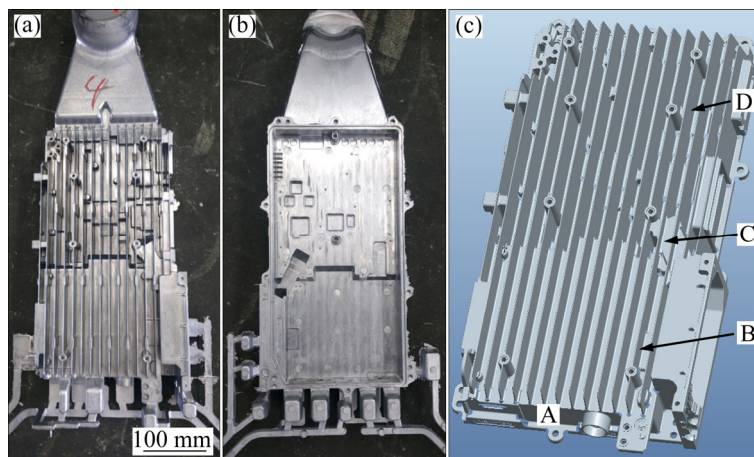


**Fig. 3** Photos of thin wall heat dissipation shells: (a) Front; (b) Back; (c) 3D map

properties, including ultimate tensile strength (UTS), yield strength (YS) and elongation to failure, were measured using a universal testing machine at room temperature. The hardness test was performed by a low load Vickers hardness tester at a load of 0.5 N. The thermal conductivity test was performed by a laser thermal conductance instrument.

Rectangular cross-sections of tensile samples were cut from the region B, and the microstructure samples of heat dissipation shells were prepared from regions A, B, C and D, as shown in Fig. 3(c). These samples were ground, polished and then etched using a 0.5% (volume fraction) solution of HF. Micrographs of samples were analyzed using Image Tool 3.0 software, where the average particle size (APS) and shape factor (ASF) were used to characterize the size and shape of primary  $\alpha_1$ -Al particles:

$$D = \sqrt{4A/\pi} \quad (1)$$

$$F = 4\pi A/P^2 \quad (2)$$

where  $P$  and  $A$  are the perimeter and area of the grain, respectively.

### 3 Results and discussion

#### 3.1 Effect of ACSR on microstructure

Figure 4 shows the quenched microstructures of the Al–8Si alloy prepared by normal casting at the pouring temperature of 660 °C and ACSR casting at the air flow of 4 L/s. Many developed dendritic particles with the size of more than 100  $\mu\text{m}$  are observed in the alloy without ACSR treatment, as shown in Fig. 4(a). However, after ACSR treatment, numerous non-dendritic  $\alpha_1$ -Al particles are distributed uniformly in liquid matrix, and the particles are much smaller and rounder in comparison to normal casting microstructure, as shown in Fig. 4(b).

#### 3.2 Effect of air flow on microstructure

Figure 5 shows the microstructures of the slurry prepared at different air flows. It can be seen that the morphology of  $\alpha_1$ -Al particles is greatly influenced by air

flows. As the air flow increases, the number of spherical particles is increased and the rosettes disappear gradually.

Figure 6 shows the variation of APS and ASF of  $\alpha_1$ -Al particles against air flow. The results indicate that APS is decreased and ASF is increased by increasing air flow. It can be concluded that excellent slurry with fine and spherical  $\alpha_1$ -Al particles can be obtained under the air flow exceeding 3 L/s, and the APS and ASF of  $\alpha_1$ -Al particles are about 40  $\mu\text{m}$  and 0.85, respectively.

It is believed that the formation of  $\alpha_1$ -Al particles in the ACSR process is ascribed to heterogeneous nucleation due to low undercooling. Under the cooling of crucible and stirring rod, the melt cools to liquidus rapidly. According to “big bang” nucleation theory [18], many effective nucleation sites, which are potential nuclei, are generated in the melt. Based on the crystal dissociating theory [19], due to the low melt temperature and constant stirring in the ACSR process, the nucleation on the wall of stirring rod and crucible, and the disengagement of nuclei also play a key role in increasing nucleation rate. In the presence of convection stirring, the temperature and solute are distributed uniformly throughout the bulk melt, and solute concentration at the solidification front is removed, so that the nuclei almost have the same growth velocity in all directions and the dendritic growth of the nuclei is restricted.

In the case of ACSR, the air flow is a key factor because it affects the morphology of  $\alpha_1$ -Al. Firstly, the cooling capacity of stirring rod increases by increasing air flow, which decreases the critical nucleation work and increases the nucleation rate of the melt. Secondly, as the air flow increases, the increase of solid fraction and the number of  $\alpha_1$ -Al decrease the distance among particles. It not only inhibits the growth of  $\alpha_1$ -Al but increases their collision frequency during stirring, and as a consequence, numerous finer and rounder  $\alpha_1$ -Al particles are obtained. Thirdly, high particle density helps the steadiness of the solid/liquid interface and keeps the spherical growth of  $\alpha_1$ -Al [20].

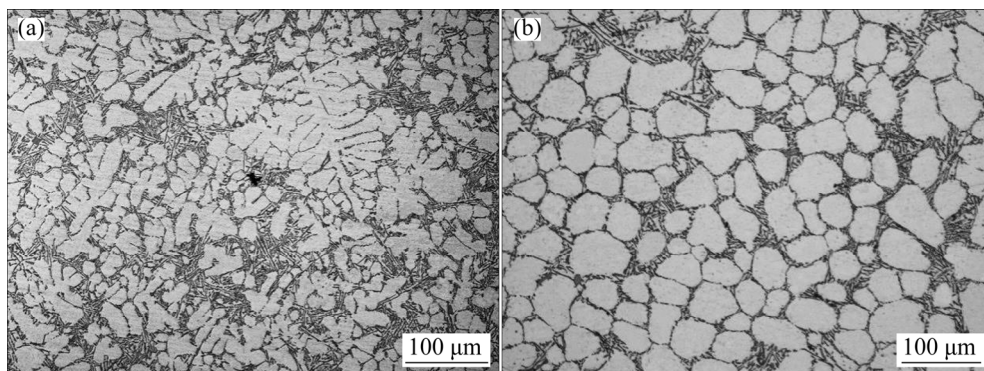


Fig. 4 Microstructures of Al–8Si alloy prepared by normal casting (a) and ACSR casting (b)

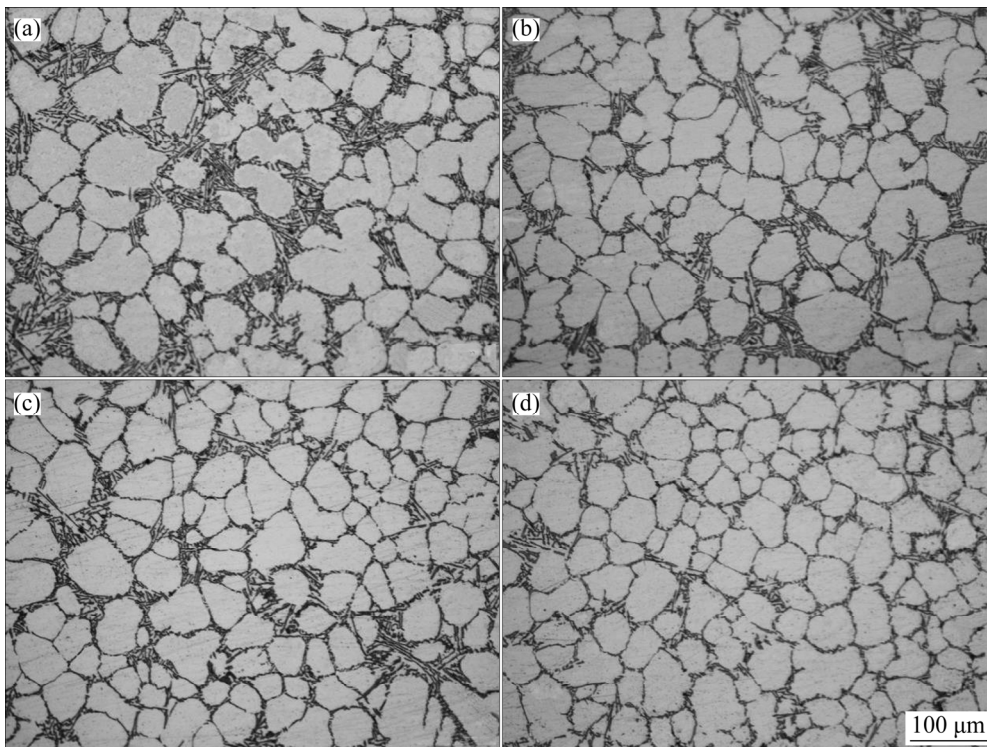


Fig. 5 Quenched microstructures of slurry of Al-8Si alloy at different air flows: (a) 0 L/s; (b) 1 L/s; (c) 3 L/s; (d) 5 L/s

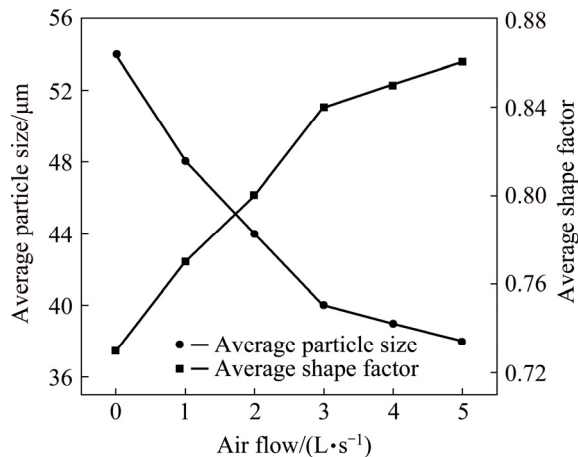


Fig. 6 Variation of APS and ASF of  $\alpha_1$ -Al particles against air flow

Figure 7 shows the microstructures of rheo-HPDC samples at the region A under air flows of 0, 1, 3 and 5 L/s. Table 1 gives the solid fraction, APS and ASF of  $\alpha$ -Al and the size of eutectic silicon of samples prepared at different air flows. When increasing the air flow from 0 to 5 L/s, the solid fraction increases from 28% to 55%,  $\alpha_1$ -Al phases are uniformly dispersed in the matrix and the APS decreases from 26 to 15  $\mu\text{m}$ , while the ASF increases from 0.71 to 0.86. It is also observed that a great number of fine  $\alpha_1$ -Al globules with the APS of below 20  $\mu\text{m}$  and the ASF of above 0.80 are observed in the samples as air flow is increased to 3 L/s. Increasing air flow to 5 L/s, a higher number of fine  $\alpha_1$ -Al particles

are observed in the samples. In fact, in the rheo-HPDC process, the primary phase in slurry is generally below 55% (volume fraction), hence the solidification of the remaining liquid of the slurry plays an important role in deciding the final mechanical properties [21].

The inset of Fig. 7 shows the eutectic silicon and  $\alpha_2$ -Al particles morphologies of rheo-HPDC samples under different air flows. By increasing air flow from 0 to 5 L/s, the APS of  $\alpha_2$ -Al particles decreases from 3.4 to 1.9  $\mu\text{m}$ , the average size of eutectic silicon decreases from 3.8 to 1.7  $\mu\text{m}$  in length, the width decreases from 0.34 to 0.26  $\mu\text{m}$ , and the aspect ratio also decreases from 11.2 to 6.5 (Table 1). It is well known that primary particles have an effect on the eutectic silicon morphology. The spherical primary particles divide the remaining liquid into some small pockets, and the eutectic reaction is limited to some small intergranular areas. This affects the nucleation of the silicon phase by changing constitutional supercooling in front of the growing eutectic grains, leading to the near-isotropic growth of silicon particles.

### 3.3 Comparison of microstructure and properties of HPDC and Rheo-HPDC samples

Figure 8 shows the microstructures observed in samples of Al-8Si alloy at different regions, by HPDC and ACSR rheo-HPDC under air flow of 5 L/s. Table 2 gives the APS and ASF of  $\alpha$ -Al particles and the average size of eutectic silicon of rheo-HPDC and HPDC

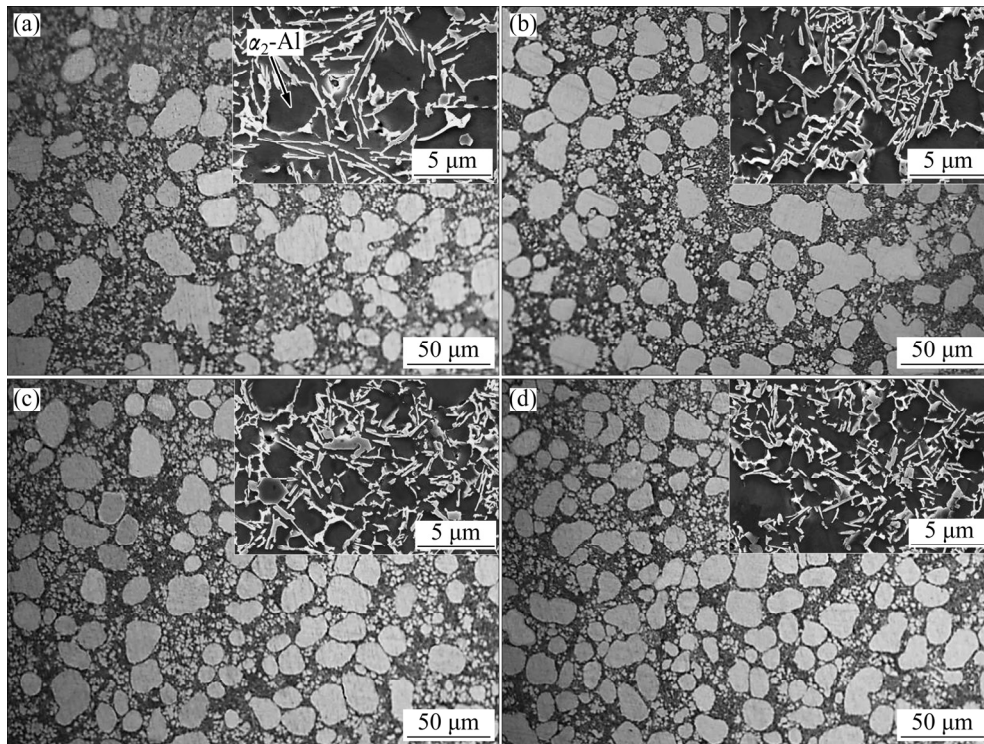


Fig. 7 Microstructures of rheo-HPDC samples under different air flows: (a) 0 L/s; (b) 1 L/s; (c) 3 L/s; (d) 5 L/s

Table 1 Solid fraction, APS and ASF of  $\alpha$ -Al particles as well as size of eutectic silicon of rheo-HPDC samples formed at different air flows

Air flow / (L·s <sup>-1</sup> )	Solid fraction/%	APS and ASF of $\alpha_1$ -Al particles		APS of $\alpha_2$ -Al particles/ $\mu$ m	Size of eutectic silicon		
		APS/ $\mu$ m	ASF		Length/ $\mu$ m	Width/ $\mu$ m	Aspect ratio
0	28	26	0.71	3.4	3.8	0.34	11.2
1	34	23	0.78	3.1	3.1	0.32	9.7
3	45	19	0.84	2.2	2.2	0.27	8.1
5	55	15	0.86	1.9	1.7	0.26	6.5

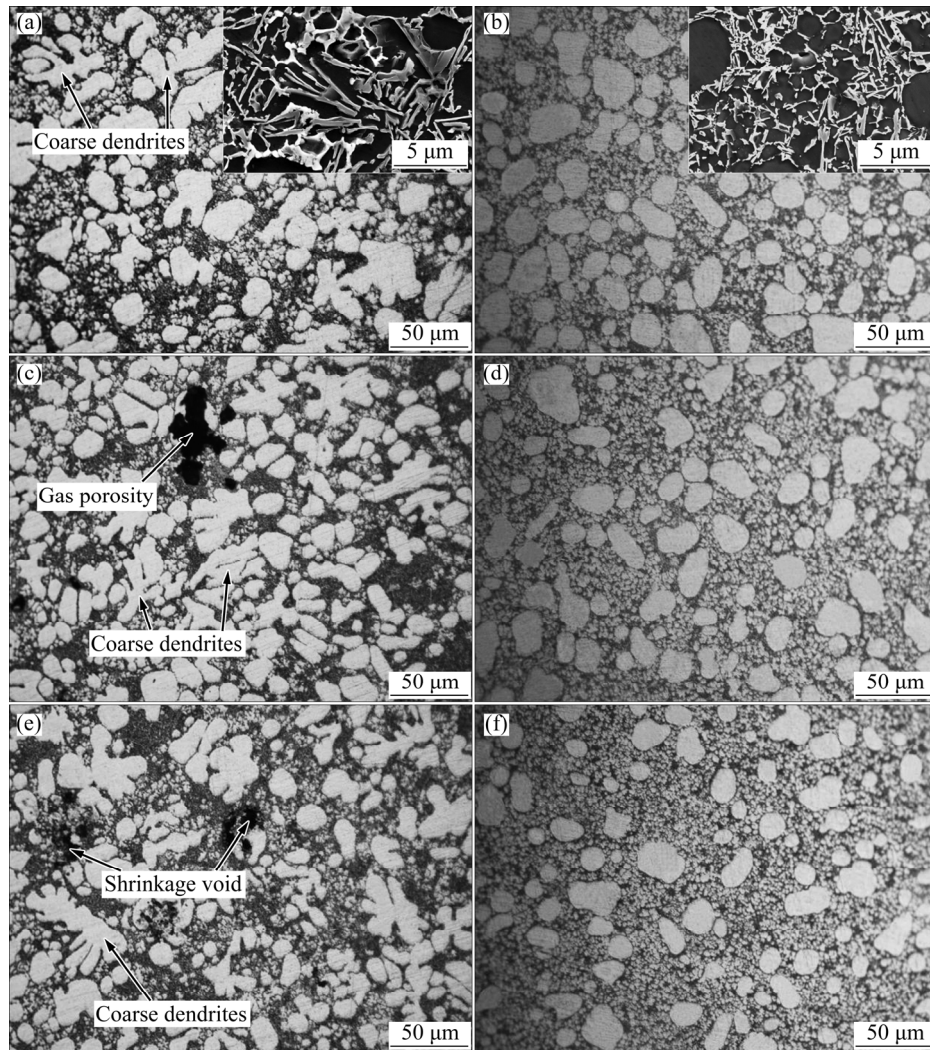
samples at the region B. Many dendrites are found in the microstructure of HPDC samples (Figs. 8(a)–(c)). The defects, such as gas porosity and shrinkage void, can be found in these three regions. However, numerous fine spherical  $\alpha_1$ -Al particles and no dendrites are found in ACSR rheo-HPDC samples (Figs. 8(d)–(f)). The solid content of rheo-HPDC samples at regions B and C is higher than that at region D due to a slower flow velocity of primary particles during filling [1,22].

Table 3 gives mechanical properties, density and thermal conductivity of samples produced by both processes. It can be seen that the higher air flow results in higher mechanical properties, density and thermal conductivity of samples, but the variation is not significant when the air flow reaches 3 L/s. The highest UTS, YS, elongation, hardness and thermal conductivity are 261 MPa, 124 MPa, 4.9%, HV 99 and 153 W/(m·K), respectively, increased by 20%, 15%, 88%, 13% and 10%, respectively, compared to liquid HPDC samples.

The improved properties, given in Table 3, show the effectiveness of the ACSR Rheo-HPDC. Such improvement can be attributed to three main reasons. One is the refinement of  $\alpha$ -Al particles (Fig. 8 and Table 2). Fine spherical primary particles help rheocasting parts to acquire improved mechanical properties [23,24]. The refinement of  $\alpha_2$ -Al within the eutectic structure has been identified as a key factor determining the proof strength of Al alloys. The fine-grained structure contributes to an increase of the YS due to the Hall–Petch effect [25]. Generally, the YS as a function of grain size can be represented by the Hall–Petch equation:

$$\sigma = \sigma_0 + Kd^{-1/2} \quad (3)$$

where  $\sigma$  is the yield stress,  $\sigma_0$  is the yield stress of a single crystal,  $K$  is a constant and  $d$  is the grain size. The grain size of Al–8Si alloy is well refined by ACSR, leading to an increase of the mechanical properties due to the Hall–Petch equation. The second reason is less shrinkage



**Fig. 8** Microstructures of HPDC (a, c, e) and ACSR rheo-HPDC (d, e, f) samples of Al-8Si alloy at different regions: (a, b) Region B; (c, d) Region C; (e, f) Region D

**Table 2** APS and ASF of  $\alpha$ -Al particles and size of eutectic silicon of rheo-HPDC and HPDC samples at region B

Process	APS and ASF of $\alpha_1$ -Al particles		APS of $\alpha_2$ -Al particles/ $\mu\text{m}$	Average size of eutectic silicon		
	APS/ $\mu\text{m}$	ASF		Length/ $\mu\text{m}$	Width/ $\mu\text{m}$	Aspect ratio
Rheo-HPDC	17	0.86	1.7	1.6	0.24	6.7
HPDC	42	0.39	4.5	4.4	0.38	11.6

**Table 3** Mechanical properties, density and thermal conductivity of samples formed by HPDC and rheo-HPDC

Process	Air flow/( $\text{L}\cdot\text{s}^{-1}$ )	Mechanical properties				Density/( $\text{g}\cdot\text{cm}^{-3}$ )	Thermal conductivity/( $\text{W}\cdot\text{m}^{-1}\cdot\text{K}^{-1}$ )
		UTS/MPa	YS/MPa	Elongation/%	Hardness (HV)		
HPDC		217	108	2.6	88	2.618	139
	0	231	112	3.2	92	2.635	143
ACSR rheo-HPDC	1	239	113	3.7	94	2.645	145
	3	255	119	4.6	97	2.660	151
	5	261	124	4.9	99	2.664	153

porosity and entrapped air (Fig. 8 and Table 3). Porosity is a negative structural factor to any casting, and the porosity of ACSR rheo-HPDC samples with density of  $2.664 \text{ g/cm}^3$  is higher than that of HPDC samples. The

improved thermal conductivity of ACSR rheo-HPDC samples is mainly due to the reduction of casting defects and the increase of density. Semisolid slurry shows distinctive pseudoplasticity and thixotropy, greatly

reducing air entrapment during filling due to a higher viscosity in contrast with the melt [4,26]. Rheo-HPDC also results in a lower solidification contraction due to a lower forming temperature. It decreases shrinkage defects especially for thin wall samples. The last reason is the refinement of eutectic silicon phase. The fine eutectic silicon which surrounds the  $\alpha$ -Al particles has greatly improved the strength and ductility of Al–Si alloy formed by rheocasting [27].

Figure 9 shows the fracture surfaces of Al–8Si alloy samples formed by HPDC and ACSR rheo-HPDC. As

shown in Fig. 9(a), several large pores are observed in the fracture surface of HPDC samples. The pores act as the fracture source while applying load to samples and accelerate the fracture process. Figure 9(b) shows a large magnification fractograph of non-hollow areas. Many flat areas, indicated by arrows in Fig. 9(b), can be observed. The fracture surfaces are mainly covered by cleavage plane. It is shown that the fracture of HPDC samples occurs generally in brittle pattern. In contrast, the fracture surfaces of samples prepared by rheo-HPDC indicate typical ductile dimple fracture mode and no pore is observed in the fractographs (Figs. 9(c) and (d)). Some tear ridges appear in the fractograph of ACSR rheo-HPDC samples which show the characteristic of ductile fracture. Thus, rheo-HPDC samples have higher mechanical properties.

#### 4 Conclusions

ACSR played a key role in the formation of non-dendritic  $\alpha_1$ -Al particles in the slurry of Al–8Si alloy, and the particles were smaller and rounder as the air flow increased. Excellent semisolid slurry of Al–8Si alloy could be obtained as the air flow exceeded 3 L/s, and the average size and shape factor of  $\alpha_1$ -Al particles were about 40  $\mu\text{m}$  and 0.85, respectively. Samples treated by ACSR at the air flow of 5 L/s had the maximum UTS, YS, elongation, hardness and thermal conductivity, which were increased by 20%, 15%, 88%, 13% and 10%, respectively, compared to the liquid HPDC samples.

#### References

- [1] JIANG Ju-fu, WANG Ying. Microstructure and mechanical properties of the semisolid slurries and rheoformed component of nano-sized SiC/7075 aluminum matrix composite prepared by ultrasonic-assisted semisolid stirring [J]. *Materials Science and Engineering A*, 2015, 639: 350–358.
- [2] ZHOU Bing, KANG Yong-lin, ZHU Guo-ming, GAO Jun-zhen, QI Ming-fan, ZHANG Huan-huan. Forced convection rheoforming process for preparation of 7075 aluminum alloy semisolid slurry and its numerical simulation [J]. *Transactions of Nonferrous Metals Society of China*, 2014, 24: 1109–1116.
- [3] SUI Yu-dong, WANG Qu-dong, YE Bing, ZHANG Li, JIANG Hai-yan, DING Wen-jiang. Effect of solidification sequence on the microstructure and mechanical properties of die-cast Al–11Si–2Cu–Fe alloy [J]. *Journal of Alloys and Compounds*, 2015, 649: 679–686.
- [4] QI Ming-fan, KANG Yong-lin, ZHOU Bing, LIAO Wan-neng, ZHU Guo-ming, LI Yang-de, LI Wei-rong. A forced convection stirring process for Rheo-HPDC aluminum and magnesium alloys [J]. *Journal of Materials Processing Technology*, 2016, 234: 353–367.
- [5] HU Zhao-hua, WU Guo-hua, ZHANG Peng, LIU Wen-cai, PANG Song, ZHANG Liang, DING Wen-jiang. Primary phase evolution of rheo-processed ADC12 aluminum alloy [J]. *Transactions of Nonferrous Metals Society of China*, 2016, 26: 19–27.
- [6] QI Ming-fan, KANG Yong-lin, ZHOU Bing, ZHANG Huan-huan, ZHU Guo-ming. Microstructures and mechanical properties of A380 aluminum alloy produced by rheo-diecasting process [J]. *The*

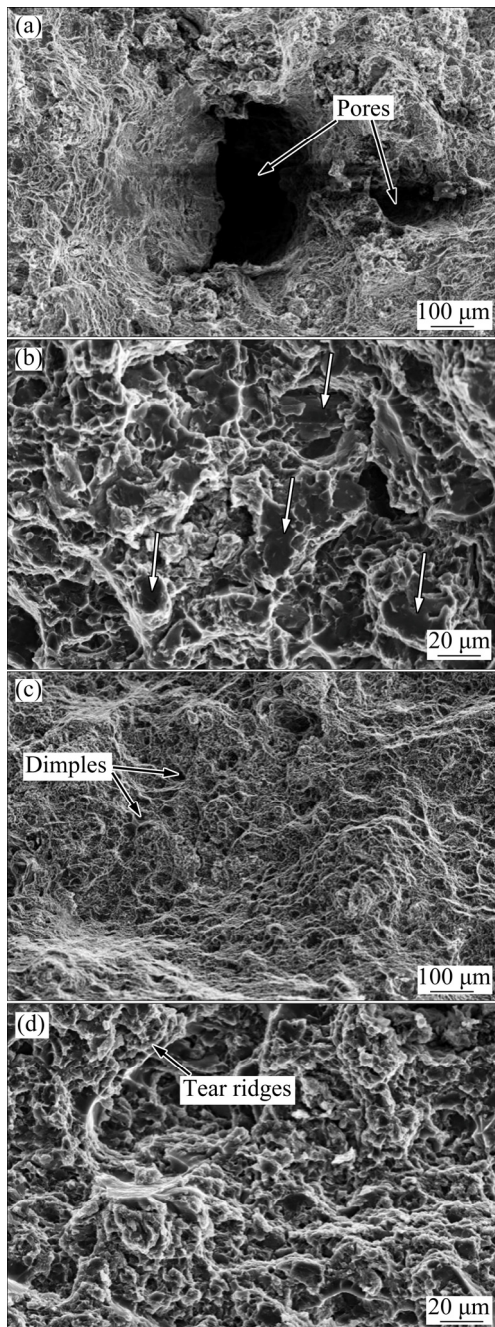


**Fig. 9** SEM fractographs of Al–8Si alloy tensile samples: (a) Low magnification, HPDC; (b) High magnification, HPDC; (c) Low magnification, rheo-HPDC; (d) High magnification, rheo-HPDC

- Chinese Journal of Nonferrous Metals, 2015, 25(8): 2029–2039. (in Chinese)
- [7] FLEMINGS M C. Behavior of metals in the semi-solid state [J]. Metallurgical Transactions A, 1991, 22: 957–981.
- [8] CHEN Zheng-zhou, MAO Wei-min, WU Zong-chuang. Mechanical properties and microstructures of Al alloy tensile samples produced by serpentine channel pouring rheo-diecasting process [J]. Transactions of Nonferrous Metals Society of China, 2011, 21: 1473–1479.
- [9] ZHAO Jun-wen, WU Shu-sen. Microstructure and mechanical properties of rheo-diecasted A390 alloy [J]. Transactions of Nonferrous Metals Society of China, 2010, 20(S3): s754–s757.
- [10] LIN Chong, WU Shu-sen, LV Shu-lin, AN Ping, WAN Li. Microstructure and mechanical properties of rheo-diecast hypereutectic Al–Si alloy with 2%Fe assisted with ultrasonic vibration process [J]. Journal of Alloys and Compounds, 2013, 568: 42–48.
- [11] ZHOU Bing, KANG Yong-lin, QI Ming-fan, ZHANG Huan-huan, ZHU Guo-ming. R-HPDC process with forced convection mixing device for automotive part of A380 aluminum alloy [J]. Materials, 2014, 7: 3084–3105.
- [12] ZHOU Bing, KANG Yong-lin, QI Ming-fan, ZHANG Huan-huan, ZHU Guo-ming. Microstructure and property of Rheo-diecasting magnesium-alloy with forced convection mixing process [J]. Solid State Phenomena, 2015, 217–218: 455–460.
- [13] LIU Zhi-yong, MAO Wei-min, WANG Wei-pan, ZHENG Zhi-kai. Preparation of semi-solid A380 aluminum alloy slurry by serpentine channel [J]. Transactions of Nonferrous Metals Society of China, 2015, 25: 1419–1426.
- [14] CHUNG I, BOLOURI A, KANG C. A study on semisolid processing of A356 aluminum alloy through vacuum-assisted electromagnetic stirring [J]. The International Journal of Advanced Manufacturing Technology, 2012, 58: 237–245.
- [15] ZHANG Yang, WU Guo-hua, LIU Wen-cai, ZHANG Liang, PANG Song, DING Wen-jiang. Microstructure and mechanical properties of rheo-squeeze casting AZ91-Ca magnesium alloy prepared by gas bubbling process [J]. Materials & Design, 2015, 67: 1–8.
- [16] ZHANG Qi, CAO Miao, CAI Jin. AlSi9Mg aluminum alloy semi-solid slurry preparation by intermediate frequency electromagnetic oscillation process [J]. Journal of Materials Processing Technology, 2015, 215: 42–49.
- [17] QI Ming-fan, KANG Yong-lin, ZHOU Bing, ZHU Guo-ming, ZHANG Huan-huan, LI Yang-de. Effects of pouring temperature and cylinder temperature on microstructures and mechanical properties of rheomoulding AZ91D alloy [J]. Transactions of Nonferrous Metals Society of China, 2015, 21: 1473–1479.
- [18] CHALMERS B. Principles of solidification [M]. New York: John Wiley & Sons, 1964.
- [19] OHNO A. Solidification-the separation theory and its practical applications [M]. Germany: Springer-Verlag Press, 1987.
- [20] YANG Liu-qing, KANG Yong-lin, ZHANG Fan, XU Jun. Microstructure and mechanical properties of rheo-diecasting AZ91D Mg alloy [J]. Transactions of Nonferrous Metals Society of China, 2010, 20: 862–867.
- [21] HITCHCOCK M, WANG Y, FAN Z. Secondary solidification behaviour of the Al–Si–Mg alloy prepared by the rheo-diecasting process [J]. Acta Materialia, 2007, 55: 1589–1598.
- [22] ZHOU Bing, KANG Yong-lin, QI Ming-fan, ZHANG Huan-huan, ZHU Guo-ming, WU Zheng-yang. Microstructure and tensile properties of AZ91D magnesium alloy by forced convection rheo-diecasting process [J]. Journal of Materials Engineering, 2014, 10: 1–5.
- [23] ZHANG Y F, LIU Y B, CAO Z Y, ZHANG Q Q, ZHANG L. Mechanical properties of thixomolded AZ91D magnesium alloy [J]. Journal of Materials Processing Technology, 2009, 209: 1375–1384.
- [24] GUAN Ren-guo, ZHAO Zhan-yong, CHAO Run-ze, ZHAO Hong-liang, LIU Chun-ming. Effects of technical parameters of continuous semisolid rolling on microstructure and mechanical properties of Mg–3Sn–1Mn alloy [J]. Transactions of Nonferrous Metals Society of China, 2013, 23: 73–79.
- [25] KUBOTA K., MABUCHI M., HIGASHI K. Review processing and mechanical properties of fine-grained magnesium alloys [J]. Journal of Materials Science, 1999, 34: 2255–2262.
- [26] ESMAILY M, SHAHABI-NAVID M, MORTAZAVI N, SVENSSON J E, HALVARSSON M, WESSEN M, JARFORS A E W, JOHANSSON L G. Microstructural characterization of the Mg–Al alloy AM50 produced by a newly developed rheo-casting process [J]. Materials Characterization, 2014, 95: 50–64.
- [27] LV Shu-lin, WU Shu-sen, DAI Wei, LIN Chong, AN Ping. The indirect ultrasonic vibration process for rheo-squeeze casting of A356 aluminum alloy [J]. Journal of Materials Processing Technology, 2012, 212: 1281–1287.

## 一种采用气冷搅拌杆流变压铸工艺制备的 Al–8Si 合金的组织与性能

祁明凡<sup>1</sup>, 康永林<sup>1,2</sup>, 朱国明<sup>1</sup>

1. 北京科技大学 材料科学与工程学院, 北京 100083;

2. 北京科技大学 材料先进制备技术教育部重点实验室, 北京 100083

**摘要:** 报道了一种新颖、高效的采用气冷搅拌杆制备半固态浆料的工艺, 该工艺通过将压缩空气不断注入到搅拌杆内腔来冷却熔体。采用该工艺制备了一种新近研发的高导热 Al–8Si 合金半固态浆料, 并将该工艺与高压铸造机结合生产出一种无线基站用薄壁散热壳体件。研究了气体流量对初生晶粒的形貌、流变压铸件的力学性能及导热系数的影响。结果表明: 当气体流量超过 3 L/s 时, 采用该工艺可以制备出优质的半固态浆料。当气体流量为 5 L/s 时, 流变压铸件的力学性能和导热系数最高, 分别为抗拉强度 261 MPa, 屈服强度 124 MPa, 伸长率 4.9%, 显微硬度 HV 99 和导热系数 153 W/(m·K)。相比于传统压铸件, 采用气冷搅拌杆流变压铸工艺生产的铸件力学性能和伸长率大大提高, 其抗拉强度、屈服强度、伸长率、显微硬度和导热系数的增长率分别为 20%、15%、88%、13%和 10%。

**关键词:** 流变压铸; Al–8Si 合金; 气冷搅拌杆; 显微组织; 力学性能; 导热系数

(Edited by Bing YANG)